

Research Article

Fracture Analysis of Compacted Clay Soil Beams with Offset Notches Based on Three-Point Bending Test: Experimental Characterization and Numerical Simulation

Liangfei Fang,^{1,2} Chengmao Cao ,^{1,2} Qing Li,^{1,2} Kuan Qin,^{1,2} Xingdong Sun,^{1,2} and Jun Ge^{1,2}

¹School of Engineering, Anhui Agricultural University, Hefei 230036, China

²Anhui Province Engineering Laboratory of Intelligent Agricultural Machinery and Equipment, Hefei 230036, China

Correspondence should be addressed to Chengmao Cao; liangfeifang@ahau.edu.cn

Received 4 November 2021; Revised 9 December 2021; Accepted 17 December 2021; Published 17 January 2022

Academic Editor: Sang-Bing Tsai

Copyright © 2022 Liangfei Fang et al. This is an open access article distributed under the Creative Commons Attribution License, which permits unrestricted use, distribution, and reproduction in any medium, provided the original work is properly cited.

The design and performance of tillage components such as subsoiler are generally characterized by the fracture features of soil mass in agricultural engineering, thus making the improvements of those tillage tools challenging due to the fact that the soil fracture mechanisms cannot be accurately explored and implemented. To alleviate this issue, in this paper, a physical three-point bending (TPB) test is conducted for investigating the fractural and fragmental characteristics of the compacted clay beams (CCB) with offset notches under the framework of mixed-mode I + II fracture, and the crack initiation as well as its propagation of the CCB is observed and fractural mechanisms of the CCB are discussed. Meanwhile, numerical simulation is also conducted utilizing two finite element methods, i.e., the extended finite element method (XFEM) and the combined finite-discrete element method (FDEM), for the CCB under three typical scenarios with notch offset ratios $C=0$, $C=0.375$, and $C=0.625$, respectively. The authenticity and availability of both experimental test and numerical simulation are validated correspondingly. Results indicate the following: (1) The average peak load, the distance between the terminal crack point and the center line of the CCB, and the average displacement will be increased with increases of the offset ratio, while initial crack angle will be decreased with increases of the offset ratio. (2) The initial crack will be extended from the bottom center of the CCB rather than the offset notch when the offset ratio is higher than 0.717. (3) The crack propagation and its mechanical properties (e.g., load-displacement curves) predicted by numerical simulation match well with those obtained from the physical test.

1. Introduction

The soil mass fracture and fragmentation caused by external forces are widely found in various agricultural cultivation/operations, such as the tillage processes by using mould-board plough, subsoiler, and sweep. The improvement with respect to the design of tillage equipment largely depends on the mechanical properties of soil mass [1, 2]. It has been reported that the crack initiation and its propagation of soil mass and formation of a desired tilth usually relied on fracture caused by the propagation of tensile cracks [3, 4]. However, the geometric discontinuities and anisotropy of the soil mass fracture processes pose difficulties for the relevant studies, and the soil fracture mechanisms are not fully revealed. Therefore, investigation on the mechanism of

soil fracture is of great significance for optimizing the design of soil engaging components, for improving the cutting performance of soil engaging tools as well as the aspect of reducing the energy consumption [5].

Nowadays, scholars have adopted tremendous testing to analyze and evaluate the fracture characteristics of the soil. Some state-of-the-art technologies and investigations could be simply summarized; for example, Zhang et al. explored the tensile fracture characteristics of the compacted soil under uniaxial tension [4]. Aluko et al. investigated the mode I fracture characteristics of the brittle agricultural soils through several TPB tests [6]. The fracture characteristics of the compacted clay were conducted using TPB test in [7–10]. Hu et al. studied the tensile fracture of the compacted clay taking advantage of experimental case and simulation case

[11]. Additionally, Jenq et al. studied the cracking process of concrete with TPB test on specimens with offset notches [12]. Guo et al. studied the I-II mixed-mode crack propagation in granite, and the conclusion that the larger the distance between the offset notch and the beam bottom center is, the larger the peak load is was obtained [13]. Zuo et al. studied the mixed-mode fracture characteristics in rocks with TPB test on specimens with offset notches [14].

However, existing studies mainly focused on analyzing the mode I fracture characteristics and fracture toughness through TPB test regarding the compacted soil with central notch, which means that the loading direction of external force is lined with the preset notch in the specimen. Few attention has been paid to the fracture characteristics and crack propagation when the soil beam specimens are examined with offset notch in TPB test. In actual engineering, the fracture behavior of soil mass is significantly impacted with natural cracks and notches in most of the scenarios, and the loading direction of external force is not lined with a natural crack [12]. Therefore, exploring the fracture characteristics and crack propagation of the soil mass in which the preset notch is not lined with the loading direction of external force is crucial to reveal the fracture mechanism of the mixed mode of the soil. In addition, fracture characteristics of the clay beam with offset notch are rarely found through TPB flexural test, from current references review. Consequently, the fracture behaviors of clay beam through TPB flexural test on specimens with offset notch need to be studied urgently.

Regarding the complex mechanism of fracture behavior of the quasibrittle materials such as soil, currently, the mainstream approach to investigate crack propagation behaviors and intrinsic fracture mechanism of the quasibrittle materials is using numerical simulation methods such as smoothed particle hydrodynamics (SPH), extended finite element method (XFEM), and the combined finite-discrete element method (FDEM). Tran et al. simulated fracture propagation of compacted clay based on a TPB flexural test with several central notches by using SPH [15]. Liu studied the crack initiation and propagation of a concrete beam based on four-point bending test by using XFEM [16]. Wang et al. simulated the onset and growth of cracks and the failure mechanism in soil slopes with XFEM [17]. Xi et al. developed a numerical method for modelling the offset notched rock beam cracking based on nonlocal extended finite element method [18]. Zhou et al. developed a 2D mesoscale model of a concrete specimen to study the dynamic tensile fracture behavior of concrete using FDEM [19]. Zhou et al. used the FDEM to simulate the evolution of a rockslide and study the failure mechanisms of rock slopes [20]. Furthermore, the fracture and damage characteristics of soils and rocks are reported utilizing the FDEM in [21, 22]. But simulation studies on the fracture characteristics of compacted clay based on XFEM or FDEM are still insufficient. Pioneer studies have demonstrated that soil has the same mechanical properties as rock, concrete, and other quasibrittle materials in terms of nonlinear postpeak softening behavior and elastic-plastic deformation characteristics [4]. Therefore, simulating/tracking the initial microcrack characteristics

and propagation behaviors of the CCB using XFEM or FDEM is a feasible technique to some extent. In particular, FDEM is a combination of finite element and discrete element method that is suitable for simulating the crack propagation behavior of nonlinear discontinuous materials such as soil.

From what has been mentioned above, the characteristics of soil type I fracture are mainly studied by experimental and simulation methods in the related literature, but there are few experimental and simulation comparative studies on soil mixed-mode I+II fracture characteristics. Given the unique mechanical property of soil mass and the improvement in the design and performance of tillage component in the cultivation operations, it is significant to explore mixed-mode I+II fracture characteristics and crack propagation behavior of the CCB; to address the above issues, the following tasks and innovation points are summarized in this paper:

- (1) The CCB specimens with offset notches under different offset ratios will be prepared; the mode I and mixed-mode I+II of fracture of the CCB are considered and discussed
- (2) The physical TPB test of CCB specimens will be conducted, in which the fracturing and crack propagation of notched clay beams with different offset ratios will be investigated
- (3) Two numerical simulation methods, namely, XFEM and FDEM, will be employed to simulate the TPB test for clay beams with offset notches, and the microlevel mechanics mechanism of fracturing and crack propagation will be furtherly explored
- (4) The applicability of two numerical simulation methods for studying the crack propagation behaviors of the CCB with several typical offset notches will be investigated and compared with the physical test

The remaining sections of this paper are organized as follows: in Section 2, the CCB specimens with different offset ratios are prepared for TPB test; in Section 3, the fracturing and crack propagation of CCB specimens in testing process are observed and discussed furtherly; in Section 4, results (e.g., the maximum principal stress nephograms, load-displacement curves) obtained from numerical simulation with respect to the XFEM and FDEM individually are presented and comparison between experimental and simulation results is analyzed. Conclusion of this paper is drawn in Section 5.

2. Experiments

2.1. Experimental Materials and Specimen Preparation.

The clay soil used in this experiment was collected from agricultural park of Anhui Agricultural University, Hefei, China. The clay was collected from 50–60 cm below the surface of the field; the physical property parameters are summarized as follows: the plasticity index $I_p = 12.1$, liquid limit $W_L = 30.2\%$, plastic limit $W_p = 18.1\%$, and maximum

dry density is $\rho = 1.85 \text{ g/cm}^3$. The particle size distribution is as follows: size $>0.25 \text{ mm}$ (11.1%), $0.1\text{--}0.25 \text{ mm}$ (18.5%), $0.075\text{--}0.1 \text{ mm}$ (33.4%), and $<0.075 \text{ mm}$ (37.0%). The clay beam specimen with offset notch used in the TPB test is shown in Figure 1. Figure 1(a) is the real experimental setup, and Figure 1(b) is the schematic diagram of TPB test. It can be seen that each CCB specimen was designed with given size $150 \text{ mm} \times 40 \text{ mm} \times 40 \text{ mm}$.

In this experiment, the original clay and 18 CCB specimens were prepared; the specific steps can be summed up as follows.

Step 1. The clay was dried and pulverized so that some unrelated stones, crop residue, and other impurities could be sieved out.

Step 2. The weight of clay was estimated according to the number of specimens and the maximum dry density, and the weight of water was calculated according to the optimum moisture content, respectively.

Step 3. The weighted water and weighted clay were well mixed, and the mixed clay was stored in a sealed bag for 24 hours.

Step 4. Two molds with the same length, width, and height, i.e., $300 \text{ mm} \times 170 \text{ mm} \times 100 \text{ mm}$, were designed, as shown in Figure 2(a).

Step 5. In order to facilitate the removal of the compacted soil in Step 7, before compaction, the internal walls of each mold were evenly coated with Vaseline and then padded with aluminum foil.

Step 6. The clay prepared in Step 3 was evenly added into the molds before being sealed and then stored for 24 hours.

Step 7. The large soil blocks were removed from the compaction molds, which were sawed into individual CCB (the number is 18) using an adjustable fixture and fretsaw, as shown in Figures 2(b) and 2(c).

Motivated by [9], the recommended notch height a (see Figure 1) to beam height W (see Figure 1) ratio a/W is set to be $0.3\text{--}0.6$. Therefore, the notch to beam height ratio (NBHR) in this experiment will be set to 0.33 ; i.e., the notch height $a = 13.3 \text{ mm}$. The offset ratio C can be calculated with the following equation:

$$C = \frac{t}{S/2} \times 100\%, \quad (1)$$

where t is the distance between the notch and center line, a is notch height, and S is the distance of two supported rollers, as shown in Figure 1.

As mentioned in [23], the result of TPB test for offset notched cemented full tailing backfilling (CFTB) demonstrated that the strength of the artificial CFTB is intermediate between the rock and soil. It is reported that the initial crack is extended from the bottom center, instead of the preset notch, when the offset ratio exceeds the given threshold,

namely, 0.75 [23]. Therefore, the specimen would not be cracked from the offset notch if the offset ratio exceeds a given threshold value. According to the suggested threshold 0.75 in [23], we then conducted two TPB tests (i.e., offset ratios $C = 0.75$ and $C = 0.733$) with the notch height $a = 13.3 \text{ mm}$; the results showed that the initial cracks of the clay beams will be extended from the bottom center rather than the preset offset notches, when the offset ratio C is set to be 0.75 ($t = 45 \text{ mm}$) and 0.733 ($t = 44 \text{ mm}$). However, when the offset ratio C is set to be 0.717 , that is to say, $t = 43 \text{ mm}$, the initial crack will be extended from the offset notch.

As discussed above, six offset ratios $C = 0.717$ ($t = 43 \text{ mm}$), $C = 0.625$ ($t = 37.5 \text{ mm}$), $C = 0.5$ ($t = 30 \text{ mm}$), $C = 0.375$ ($t = 22.5 \text{ mm}$), $C = 0.25$ ($t = 15 \text{ mm}$), and $C = 0$ ($t = 0 \text{ mm}$) will be therefore conducted. In this experiment, 18 specimens were prepared and then divided into 3 groups; i.e., $C0.717\text{-}G1\text{-}G2\text{-}G3$: 3 specimens are prepared for offset ratio 0.717 , $C0.625\text{-}G1\text{-}G2\text{-}G3$: 3 specimens are prepared for offset ratio 0.625 , $C0.5\text{-}G1\text{-}G2\text{-}G3$: 3 specimens are prepared for offset ratio 0.5 , $C0.375\text{-}G1\text{-}G2\text{-}G3$: 3 specimens are prepared for offset ratio 0.375 , $C0.25\text{-}G1\text{-}G2\text{-}G3$: 3 specimens are prepared for offset ratio 0.25 , and $C0\text{-}G1\text{-}G2\text{-}G3$: 3 specimens are prepared for offset ratio 0 . Each specimen is labeled according to its offset ratio. For example, a specimen in group 3 with the offset ratio 0.5 would be labeled with $C0.5\text{-}G3$. The notches were formed with a fretsaw, and the width of the notches was formed with 1.6 mm . Figure 3 shows the six prepared specimens with above six offset ratios.

2.2. Experimental Setup and Procedures. The CCB fractural experiment was conducted in Anhui Province Engineering Laboratory of Intelligent Agricultural Machinery and Equipment at Anhui Agricultural University, Hefei, China. The loading force F in the TPB test was oriented horizontally to eliminate the effect of gravity of the CCB specimen [7, 10]. The overview of experimental setting is displayed in Figure 4. Specifically, Figure 4(a) is the whole testing system for testing soil fracture mechanical properties, including data acquisition module, servomotor, and some specific experimental subrigs of mechanical properties test platform which are presented in Figure 4(b) in detail. The support plate equipped with universal rollers is coated with Vaseline to reduce the friction effect during experimental testing. The loading rate of servomotor is 0.6 mm/min . The industrial-grade PLC control unit shown in Figure 4(a) was used for collecting experimental data such as load and the displacement of loading point P during the loading process.

3. Results and Analysis

3.1. Crack Propagation Characteristics. Figure 5(a) shows the crack propagation morphology of three specimens, i.e., $C0\text{-}G1$, $C0\text{-}G2$, and $C0\text{-}G3$ (from top to bottom), with offset ratio $C = 0$, in the framework of type I fractures. The crack propagation paths of the three specimens are not exactly a straight line, but zigzagged toward loading point P . From Figure 5(a), it can be seen that all terminal cracks point

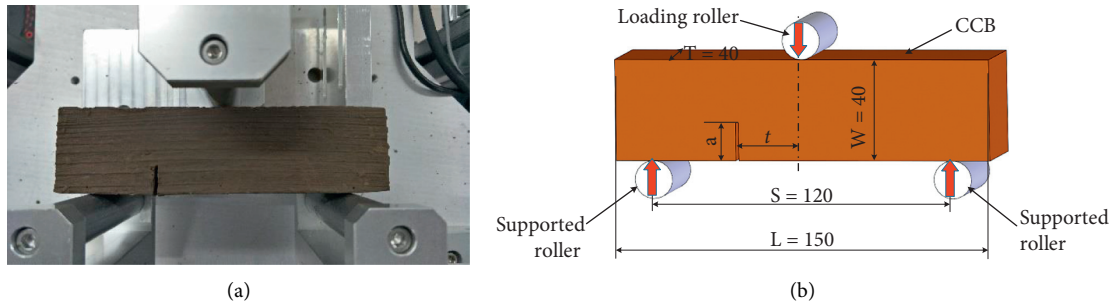


FIGURE 1: The CCB specimen with offset notch used for TPB test. (a) Experimental setup; (b) the schematic diagram of TPB test.

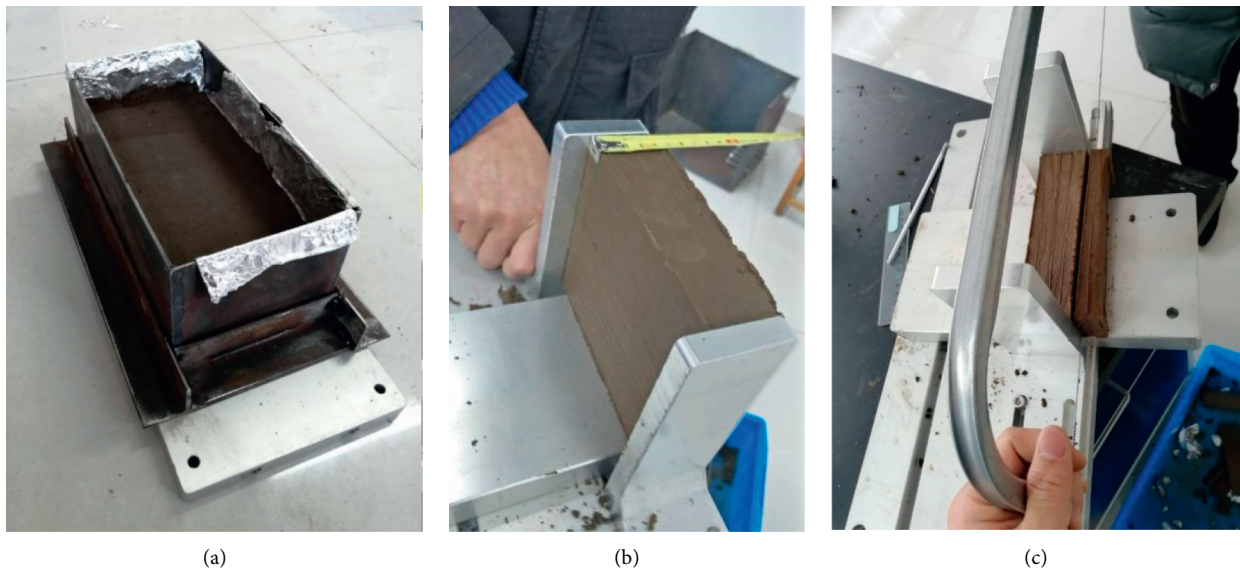


FIGURE 2: (a) The molds for compacting clay; (b) the adjustable fixture; (c) cutting soil blocks by fretsaw.



FIGURE 3: The prepared CCB specimens with different offset notches: $C = 0.717$ ($t = 43$ mm), $C = 0.625$ ($t = 37.5$ mm), $C = 0.5$ ($t = 30$ mm), $C = 0.375$ ($t = 22.5$ mm), $C = 0.25$ ($t = 15$ mm), and $C = 0$ ($t = 0$ mm).

(TCP) in crack propagation morphology will be close to the loading point when the specimens are completely cracked, which are similar to the ones obtained from the typical soil specimen with a centered notch in [6], as presented in Figure 5(b). The reason for the zigzagging crack propagation

paths of specimens with offset ratio $C = 0$ may be determined by the inhomogeneity and quasibrittle nature of the soil material.

Figure 6 shows the typical crack propagation of the given specimens with offset ratios $C = 0.375$ (see left subfigure) and

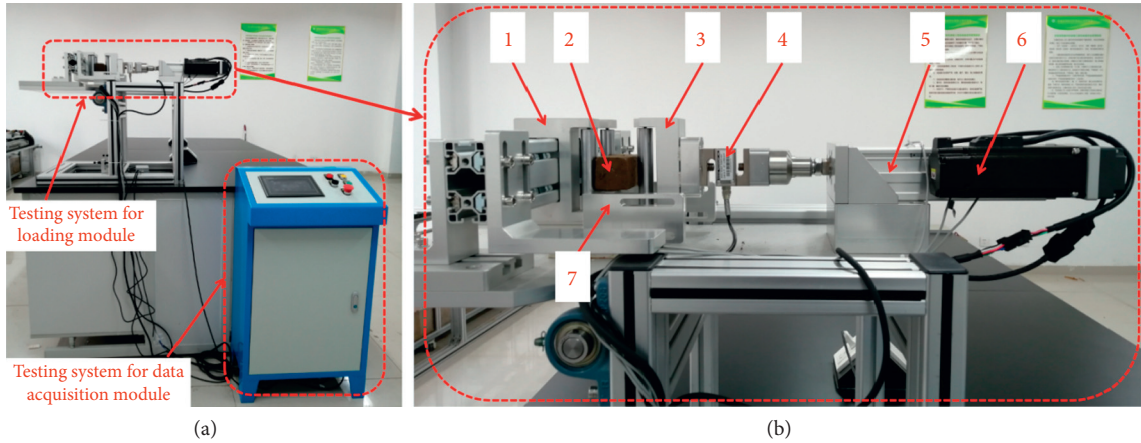


FIGURE 4: Experimental testing system of the TPB test on compacted clay. (a) The whole testing system; (b) mechanical properties test platform, in which label 1 is the adjustable support frame, label 2 is the CCB specimen, label 3 is the loading point, label 4 is a pressure transducer, label 5 is the electric cylinder, label 6 is the servomotor, and label 7 is the support plate.

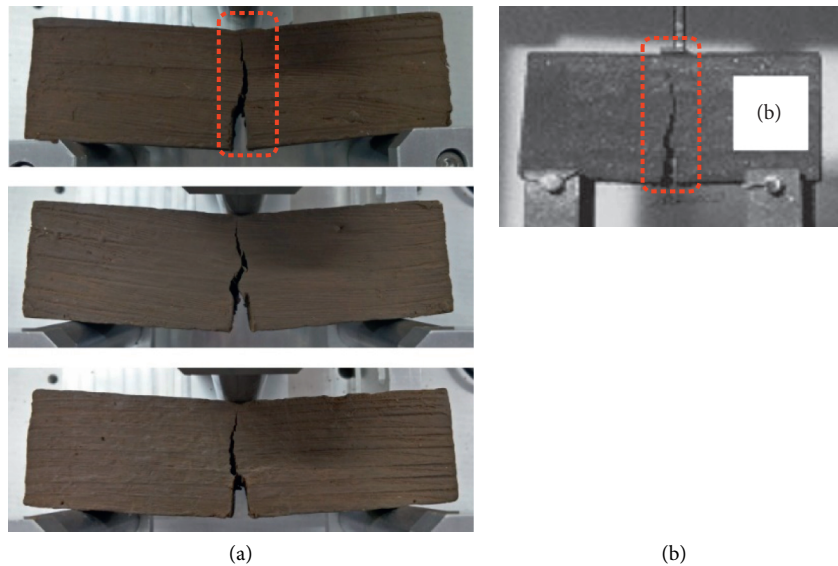


FIGURE 5: Crack propagation morphology in the group with offset ratio $C = 0$. (a) Results of this experiment: C0-G1, C0-G2, and C0-G3 (from the top to the bottom); (b) result of crack propagation morphology in [6].

$C = 0.625$ (see right subfigure), respectively. The process of crack propagation can be divided into four stages: **In stage 1**, the initial crack appeared at the end of the offset notch and started propagating toward the loading point. The angle between the initial crack direction and the line perpendicular to the direction of the load is defined as the initial crack angle θ , as shown in Figure 7. According to Figures 6(a) and 6(b), the initial crack angle θ shows a decreasing trend as the offset ratio increases, which is consistent with the experimental results reported in [23]. **In stages 2 and 3**, the crack propagation paths are slightly zigzagged and the crack still propagated toward the loading point P . However, different trends of the crack propagation paths are discovered **in stage 4**. For example, the terminal crack in specimens with offset ratio $C = 0.375$ almost pointed to loading point P , while the terminal crack in specimens with offset ratio $C = 0.625$ deviated significantly from loading point P . In this paper, the

distance between the terminal crack and the center line of the CCB is denoted by symbol X (see Figure 8). These crack propagation characteristics are in agreement with the results in [13]. Similar crack propagation characteristics are also observed from other groups, and similar phenomena will not be repeated.

Figure 9 shows the evolution trends of θ and X versus the offset ratio C . As shown in Figure 9(a), the average initial crack angle (AICA) decreases approximately and linearly as the offset ratio C increases from 0.25 to 0.717, indicating that the larger the offset ratio, the flatter the initial crack. Initial crack angles θ are discrete when the offset ratio reaches 0.717, which is close to the given threshold. As shown in Figure 9(b), it can be seen that the average value of X increases gradually with the increase of the offset ratio C , but the value of X increases significantly when the offset ratio increases from $C = 0.5$ to $C = 0.625$.

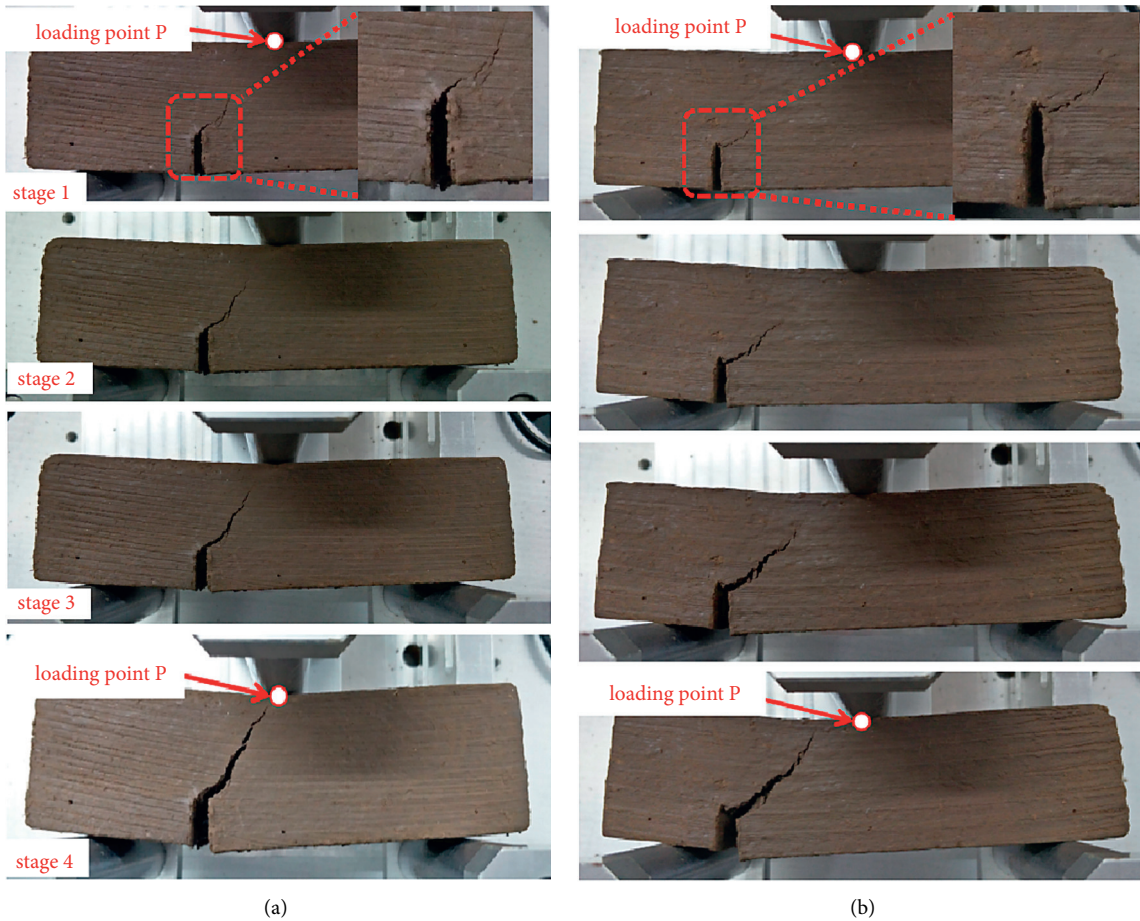


FIGURE 6: Typical crack propagation morphology in four stages during the loading process. (a) $C=0.375$; (b) $C=0.625$.

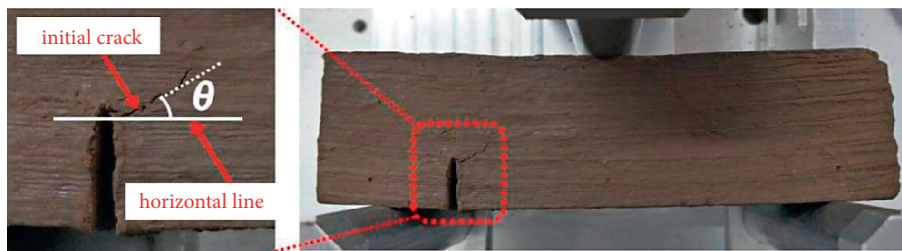


FIGURE 7: The initial crack angle θ with the offset ratio $C \neq 0$.

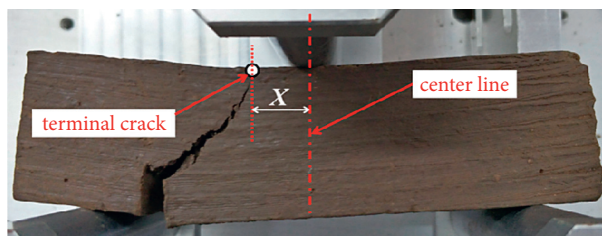


FIGURE 8: The distance from the terminal crack to the center line of the CCB with offset ratio $C \neq 0$.

3.2. *Load-Displacement Curves.* The load-displacement curves obtained from six offset ratios are shown in Figure 10. The load-displacement curve can be typically divided into

three stages, as shown in Figure 11. **In the first stage** (1→2), the load F increases approximately and linearly with the increases of displacement of loading point P .

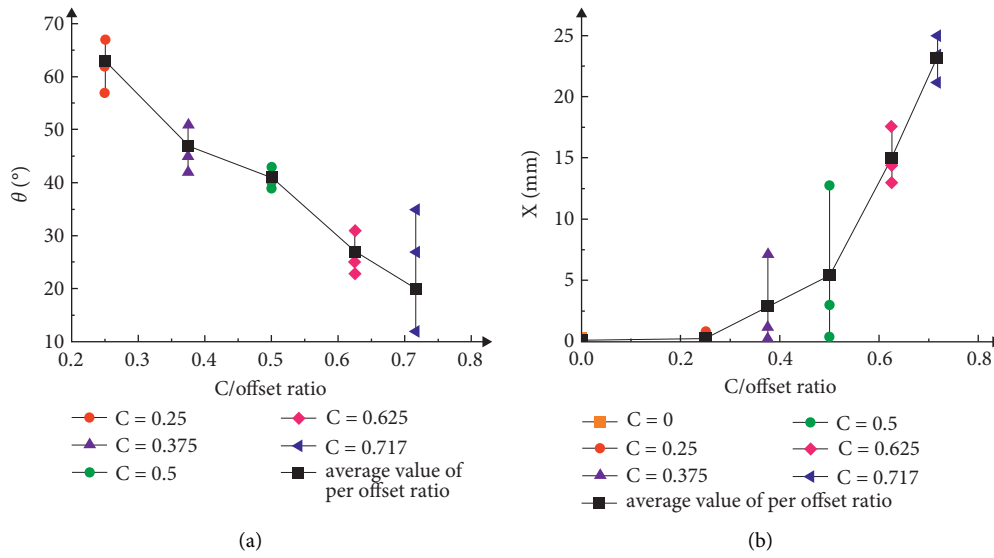


FIGURE 9: The trends of θ and X in the specimens with the increase of offset ratio C . (a) Initial crack angles θ vs. offset ratio C ; (b) the distance between the terminal crack point and the center line (X) vs. offset ratio C .

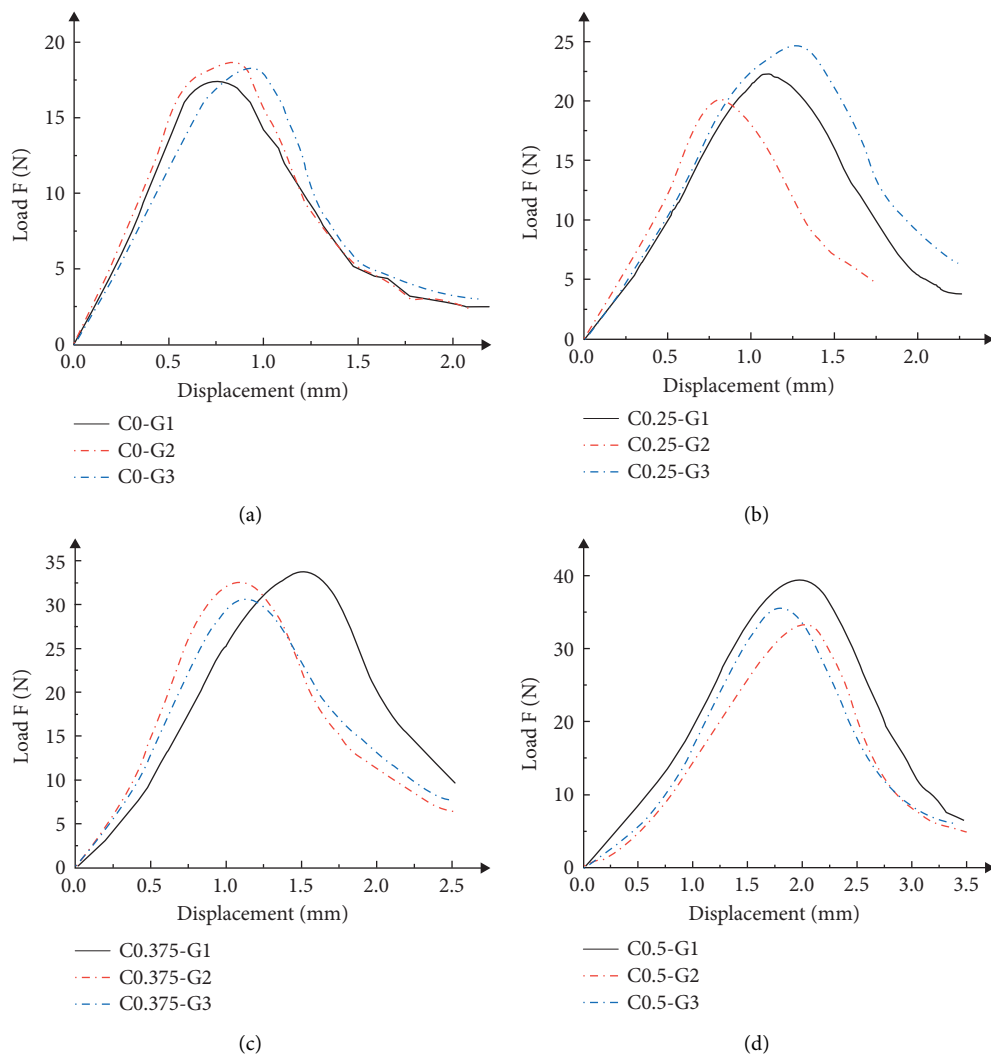


FIGURE 10: Continued.

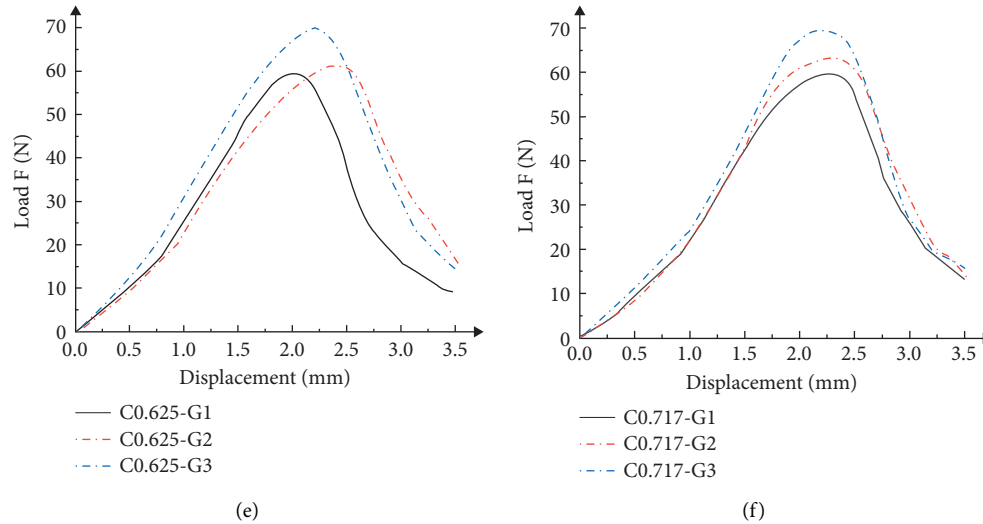


FIGURE 10: The load-displacement curves of six offset ratios of TPB test: (a) $C = 0$; (b) $C = 0.25$; (c) $C = 0.375$; (d) $C = 0.5$; (e) $C = 0.625$; and (f) $C = 0.717$.

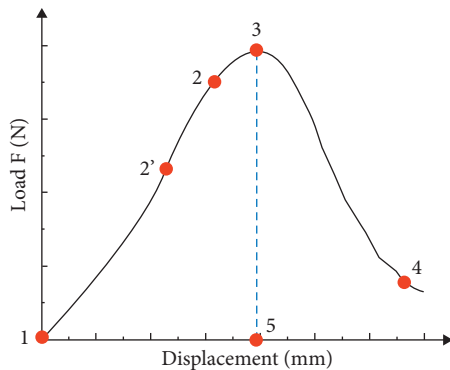


FIGURE 11: Typical load-displacement curve of the TPB test for CCB.

Therefore, the first stage can be regarded as the linear elasticity stage. **For the second stage** ($2 \rightarrow 3$), the load F increases nonlinearly with the increases of displacement of the loading point P . Thus, the second stage can be regarded as the nonlinear strengthening stage, where the load reaches the peak value F_{\max} and when the curve reaches point 3. **For the third stage** ($3 \rightarrow 4$), the load F gradually decreased with the increases of displacement of loading point P . Thus, the third stage can be regarded as the nonlinear postpeak softening stage. The postpeak strain softening behavior may be related to the plastic deformation of the soil materials and residual stresses.

According to Figure 11, the trend and shape of the load-displacement curves under different offset ratios are similar to those under the offset ratio of zero, and all load-displacement curves have three stages, i.e., $1 \rightarrow 2$, $2 \rightarrow 3$, and $3 \rightarrow 4$, which is in agreement with the descriptions in [7] and [8]. However, Figures 10(b)–10(f) reveal that the load-displacement curves go through two more distinct sub-stages $1 \rightarrow 2'$ and $2' \rightarrow 2$ during stage $1 \rightarrow 2$. At substage $1 \rightarrow 2'$, the load-displacement curves become steeper with

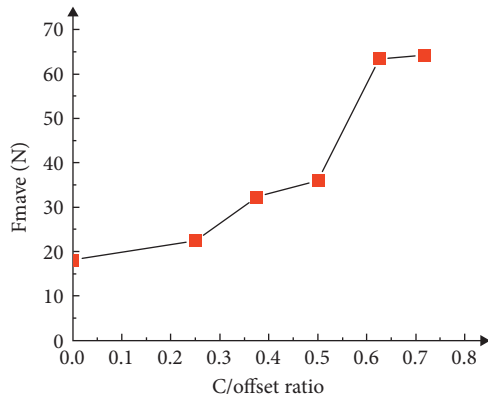
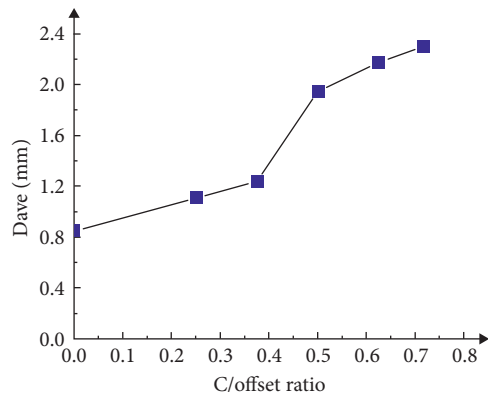
the increases of the displacement; we may call the substages $1 \rightarrow 2'$ a concave stage. The reason that induced the concave stage is the type of fracture changed from mode I to I-II mixed mode due to shear stress of cross section of given fracture. The initial microcracks usually formed in weak regions of the stress concentration, and these microcracks cannot run through following the direction of the specimen's thickness T . As the load increases, these microcracks will be gradually accumulated around the notch, but the accumulated energy is not enough to form an overall fracture surface [14]. At substage $2' \rightarrow 2$, the slopes of the curves approach a constant value, which fell in an elastic deformation stage, and this is also the stage of strain energy accumulation. The accumulated microcracks are not completely instable until undergoing the nonlinear strengthening stage $2 \rightarrow 3$, before the loading force reaches stage $2 \rightarrow 3$, as shown in Figures 10(b)–10(f). However, concave characteristic of load-displacement curves is not obvious in substages $1 \rightarrow 2'$ such as curve of C0.375-G3 in Figure 10(c), because the nonhomogeneity and non-continuity of the soil mass affect its mechanical properties at the microscopic scale to some extent.

Table 1 summarizes the tested results of mechanical properties including the peak load (i.e., maximum load) and the displacement at maximum load, where F_{\max} denotes the peak load, F_{mave} denotes the average peak load, D denotes the displacement at the peak load, and D_{ave} denotes the average value of D .

Figure 12 shows the trend of the average peak load F_{mave} versus different offset ratios, and Figure 13 shows the trend of the average displacement, namely, D_{ave} versus different offset ratios. As can be seen from Figure 12, the average peak load generally increases with the increase of the offset ratio. When the offset ratio increases from $C = 0$ to $C = 0.5$, the average peak load is increased slightly, showing an approximately linear increasing trend. However, when the offset ratio increases from $C = 0.5$ to $C = 0.625$, the average

TABLE 1: The tested results of mechanical properties.

| Specimen label | Offset ratio C | Maximum load F_{max} (N) | Average maximum load F_{mave} (N) | The displacement at maximum load D (mm) | The average displacement at maximum load D_{ave} (mm) |
|----------------|----------------|----------------------------|-------------------------------------|---|---|
| C0-G1 | | 17.46 | | 0.77 | |
| C0-G2 | 0 | 18.70 | 18.15 | 0.83 | 0.85 |
| C0-G3 | | 18.30 | | 0.96 | |
| C0.25-G1 | | 22.35 | | 1.18 | |
| C0.25-G2 | 0.25 | 20.27 | 22.44 | 0.81 | 1.10 |
| C0.25-G3 | | 24.71 | | 1.31 | |
| C0.375-G1 | | 33.67 | | 1.49 | |
| C0.375-G2 | 0.375 | 32.58 | 32.33 | 1.09 | 1.24 |
| C0.375-G3 | | 30.75 | | 1.14 | |
| C0.5-G1 | | 39.40 | | 1.99 | |
| C0.5-G2 | 0.5 | 33.45 | 36.13 | 2.06 | 1.95 |
| C0.5-G3 | | 35.53 | | 1.80 | |
| C0.625-G1 | | 59.12 | | 2.01 | |
| C0.625-G2 | 0.625 | 60.78 | 63.40 | 2.34 | 2.18 |
| C0.625-G3 | | 70.31 | | 2.19 | |
| C0.717-G1 | | 59.68 | | 2.30 | |
| C0.717-G2 | 0.717 | 63.26 | 64.16 | 2.38 | 2.30 |
| C0.717-G3 | | 69.55 | | 2.22 | |

FIGURE 12: F_{mave} vs. offset ratio C .FIGURE 13: D_{ave} vs. offset ratio C .

peak load will be increased rapidly, approximately two times than the values compared with that generated from the scenario with $C=0.5$. As the offset ratio increases from $C=0.625$ to $C=0.717$, the average peak load remains almost

unchanged. Therefore, the point where the offset ratio is 0.5 can be treated as a mutation point of F_{mave} . With the increase of the offset ratio, the fracture mode shifts from type I to mixed mode, and the average peak load increases slower as the offset ratio approaches the threshold of 0.717. According to Figure 13, the average displacement of the loading point also increases with the increases of the offset ratio. When offset ratio C increases from 0.375 to 0.5, D_{ave} is increased significantly. When the offset ratio C increases from 0.5 to 0.717, the variation tendency of D_{ave} value is becoming slow, and the increase rate is close to that of D_{ave} value when C increases from 0 to 0.375.

3.3. Fracture Mechanism of the CCB with Offset Notch. As shown in Figure 12, under a constant notch height a , the average peak load increases with the increase of the offset ratio. The fracture mode shifts from mode I to mixed mode under a nonzero offset ratio. Therefore, the changes of peak load can directly reflect the changes of fracture resistance in the specimen. In this paper, the specimens in the TPB test can be regarded as simply supported beam, as shown in Figure 14.

According to the equilibrium of moments, we have

$$F_A = F_B = \frac{F}{2}, \quad (2)$$

$$M = F_A \left(\frac{S}{2} - t \right), \quad (3)$$

where F is the load, F_A and F_B are the support reactions of two symmetrical supports of the soil beam, respectively, M is the bending moment of the cross section where the notch is located, and S is the effective span of the beam. Since the cross section of the clay beam specimen is rectangular, the bending moment of the cross-section where the notch is located can be expressed with the following equation, where

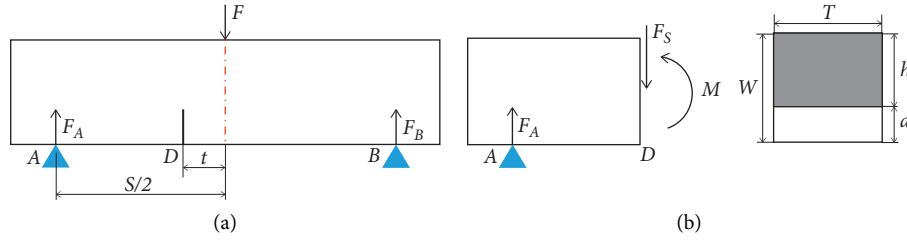


FIGURE 14: The schematic diagram of the CCB with offset notch. (a) The diagram of the CCB; (b) the cross section of fracture.

the effective height of the cross section can be expressed in terms of $h = W - a$.

$$M = \frac{EWh^3}{12\rho}. \quad (4)$$

According to (2) and (3), although the load F is gradually increased with the increases of offset ratio C , the bending moment of the cross section is decreased. As the shear force F_s of the cross section is constant, the shear stress remains unchanged and the bending stress gradually decreases. Under a constant notch height, the specimen is cracked from the bottom center instead of the notch when the offset ratio

exceeds 0.717. When the offset ratio is less than the given threshold, the bending stress in the cross section where the notch is located is greater than that in the central cross section of the specimen. Therefore, the specimen will be cracked from the initial notch when the bending stress is satisfied to the strength of the specimen.

The soil stress intensity factor K_I can be determined using the following equation [7, 9]:

$$K_I = \frac{FS}{BW^{3/2}} f\left(\frac{a}{W}\right), \quad (5)$$

where f is a function of a/W and is expressed as

$$f\left(\frac{a}{W}\right) = \frac{3(a/W)^{1/2} [1.99 - (a/W)(1 - (a/W))(2.15 - 3.93(a/W) + 2.7(a/W)^2)]}{2(1 + 2a/W)(1 - (a/W))^{3/2}}. \quad (6)$$

When F reaches the peak load, the mode I fracture toughness (K_{IC}) of the material can be determined using (5). The fracture toughness K_{IC} can be calculated when the average peak load F_{mave} at the offset ratio $C = 0$ is substituted into the load F in (5), and the value of the fracture toughness is $11.1 \text{ kPa}\cdot\text{m}^{0.5}$. The average tensile strength (σ_t) of the specimens is measured as 25.9 kPa using the direct tension testing method and 8-shaped fixture. Thus, the fracture toughness to tensile strength ratio K_{IC}/σ_t of the specimens in this experiment is 0.4286, which is close to the one reported in [10].

4. Simulation Results and Analysis Using XFEM and FDEM

In this section, two 2D simulation models will be established using XFEM and FDEM, and then the model parameters of two 2D simulation models are given accordingly. The simulation results including crack propagation path and load-displacement curves for TPB test of the CCB with offset notches under the offset ratios, $C = 0$, $C = 0.375$, and $C = 0.625$, as three typical cases, will be presented in detail.

The XFEM has low dependence on the mesh and does not require mesh reconstruction for crack propagation or mesh refinement at crack tips, which solves discontinuous mechanical problems such as crack propagation based on the idea of independent meshing. Additionally, the XFEM identifies the initial cracks according to the maximum

principal stress criteria [24]. When the damage initiation criterion is satisfied, the specimen enters the damage evolution phase and crack propagation starts. Damage evolution laws include the ones based on displacement and the ones based on energy, and the power law is adopted:

$$f = \frac{\langle \sigma_{\max} \rangle}{\sigma_{\max}^0}, \quad (7)$$

$$\left\{ \frac{G_I}{G_{IC}} \right\} + \left\{ \frac{G_{II}}{G_{IIC}} \right\} + \left\{ \frac{G_{III}}{G_{IIIC}} \right\} = 1, \quad (8)$$

where σ_{\max} is the maximum principal stress, σ_{\max}^0 is the critical maximum principal stress, and cracks initiate when $f = 1$. In (8), G_I , G_{II} , and G_{III} are the fracture energy, and G_{IC} , G_{IIC} , and G_{IIIC} are the critical fracture energy. The detailed XFEM theory can be found in [17, 24, 25].

The FDEM was originally proposed by Munjiza et al. [26]; it can be used for simulating the failure and fracture behaviors of brittle and quasibrittle materials. In recent years, the FDEM has been adopted to simulate deformation, cracking, and crack propagation in rocks and soil [19–22, 27]. With FDEM, the soil mass can be idealized as a collection of deformable elements and cohesive elements, where the deformable elements are bonded by the cohesive elements. The deformable elements are assigned the soil material properties and the cohesive elements are assigned the bonding properties. The continuous behaviors of soil materials are facilitated by constitutive relation of the

deformable elements and the stiffness of the cohesive elements, and the noncontinuous behaviors are facilitated by the cohesive elements [20].

Figure 15 shows the crack propagation process of a two-dimensional FDEM model with the deformable elements represented by triangular elements and the cohesive elements represented by four-node elements. In the FDEM model, as shown in Figure 16, every two adjacent triangular elements are connected with one four-node cohesive element (FNCE). The advantage is that cracks can be propagated along the arbitrary paths instead of straight lines. Therefore, the simulated soil crack propagation paths and cracking characteristics will be more realistic. The detailed FDEM theory can be found in [20, 24, 27].

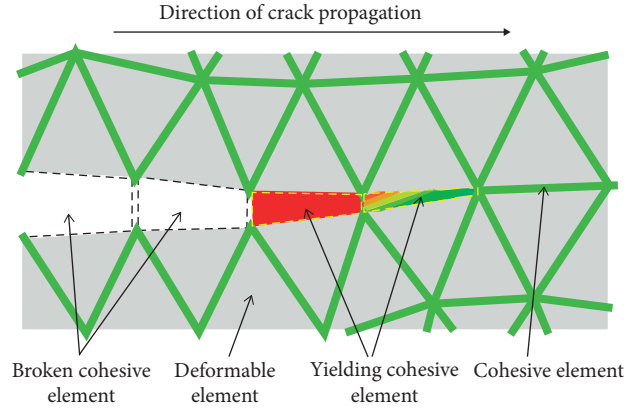


FIGURE 15: The simulated crack propagation process with FDEM.

4.1. Models Development and Parameters Setting. The models are built with 2D shell elements, and the geometry of the model is the same as that of the specimen shown in Figure 1. The two lower supports and the upper loading point are set as discrete rigid bodies (DRB). Preliminary experiments were conducted to investigate the effect of grid sensitivity on the peak load and load-displacement curves and then the appropriate mesh size could be determined. Considering the economy of calculation, in this paper, the 1.8 mm CPS4R elements are selected for XFEM, making it a total number of 6980 elements. The viscosity control factor is set to be 0.001 to improve the convergence of the calculation, and the loading displacement is set to be 3 mm.

Because the commercial finite element software ABAQUS has no function to automatically insert cohesive element between all solid elements, the insertion of zero-thickness cohesive elements between triangular solid elements in the crack propagation region will be achieved by *Python* script developed in this paper. The geometry of the FDEM simulation is consistent with the XFEM simulation, the lower supports and upper loading point are discrete rigid bodies as well, and quasistatic analysis was adopted [20]. Preliminary experiment showed that mesh size has a large influence on the FDEM calculation results. The deformable elements are represented with 1 mm CPS3 elements to ensure the simulation accuracy, and the number of mesh is 12378. Cohesive elements are inserted globally between the adjacent deformable elements to simulate the discontinuity of crack propagation and the randomness of crack propagation paths in quasibrittle soil materials. The cohesive elements are represented with COH2D4 elements with a thickness of zero, and the number of mesh is 18365. The FDEM simulation model with offset ratio is shown in Figure 16.

Generally, soil mass has complex physical and mechanical properties, and compacted clay has the properties of a quasibrittle material. Since the plastic behavior of clay needs to be considered in the simulation, the material properties of the deformable elements in the XFEM and FDEM models should be described by the elastoplastic constitutive model of clay. In this paper, the deformable elements are employed via D-P constitutive model, which was also applied in [28–30], and the parameters of the material are borrowed from [29].

Soil mass fracture parameters are critical for the simulation of crack propagation in clay beams. The nominal stress σ_n can be calculated with the following equation following [18, 31] and regarded as the reference to set the values of maximum principal stress (Maxps) and maximum stress (Maxs) in this simulation:

$$\sigma_n = \frac{\sigma_t}{\sqrt{1 + (l_e/l_{fpz})}}, \quad (9)$$

where l_e is the equivalent crack length, which can be calculated using the first following equation, and symbol l_{fpz} is the length of the fracture propagation area, which can be calculated using (11):

$$l_e = \frac{a(1-\lambda)^2 G(\lambda)}{1.12}, \quad (10)$$

$$G(\lambda) = \frac{1.99 - \lambda(1-\lambda)(2.15 - 3.93\lambda + 2.7\lambda^2)}{\sqrt{\pi}(1+2\lambda)(1-\lambda)^{3/2}},$$

where a is the notch height and λ is the notch height to specimen height ratio. The length of the fracture propagation area is given by

$$l_{fpz} = \left(\frac{K_{IC}}{2\sigma_t} \right)^2, \quad (11)$$

where K_{IC} is the fracture toughness and σ_t is the tensile strength.

The XFEM and FDEM simulation models with respect to offset ratios, $C = 0$ and $C = 0.5$, are prebuilt firstly. The model parameters are debugged by inverse analysis, and the trial-and-error method is used manually to calibrate simulation parameters. The simulation parameters of soil mass fracture initiation and damage evolution are obtained following the load-displacement curves shown in Figures 10(c) and 10(e) (see Section 3.2). For the XFEM and FDEM simulation, the fracture and damage parameters in the normal and tangential directions are assumed identically [18, 19]. Finally, all material parameters for the simulations are summarized in Tables 2 and 3.

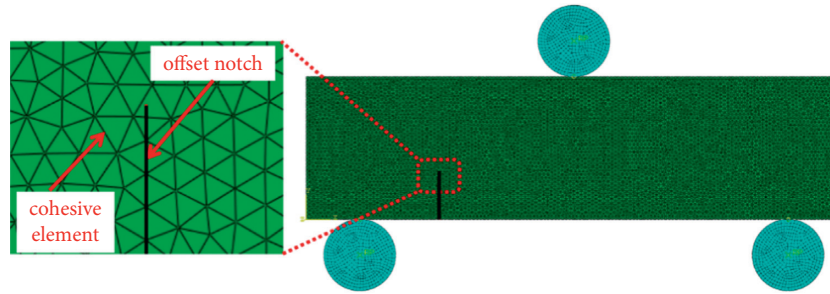


FIGURE 16: The FDEM simulation model.

TABLE 2: The D-P constitutive model parameters of the soil mass.

| Parameters | Density (kg/m ³) | Young's modulus (Pa) | Poisson's ratio | Friction angle (°) | Stress ratio | Dilation angle (°) | Soil moisture (%) |
|------------|------------------------------|----------------------|-----------------|--------------------|--------------|--------------------|-------------------|
| Value | 1790 | 1.14×10^6 | 0.3 | 12.21 | 1 | 0 | 20.03 |

TABLE 3: The parameters for the XFEM and FDEM simulations.

| Parameters | Maximum principal stress (Pa) $C = 0.375$ | Maximum principal stress (Pa) $C = 0.625$ | Fracture energy (J) | Nominal stress (Pa) | Elastic/Enn/Ess/Ett |
|------------|--|--|---------------------|---------------------|---------------------|
| XFEM | 3200 | 3400 | 0.7 | — | — |
| FDEM | — | — | 1 | 6500 | 1.5×10^8 |

4.2. Simulation Results and Analysis. Figures 17 and 18 show the maximum principal stress nephograms (MPSN) of the crack propagation process for the CCB with offset ratio $C = 0.625$ using the XFEM and FDEM, respectively. The crack propagation paths and directions are similar to those from the above physical test; for example, the distances from terminal crack to loading point P are similar to those obtained from the physical test. However, as shown in Figures 17(a) and 18(a), the initial crack angle θ at the crack initiation stage is larger than that from the actual test. The main reason is that the normal and tangential simulation parameters are set to the same value.

Figure 19 depicts the load-displacement curves from the simulations and physical test with offset ratios $C = 0$, $C = 0.375$, and $C = 0.625$. In both cases, the shapes and trends of the load-displacement curves from the XFEM and FDEM simulations under the offset ratios $C = 0$, $C = 0.375$, and $C = 0.625$ are generally similar with those of the experimental results. As shown in Figure 19(a), the load-displacement curves under the offset ratios $C = 0$ obtained from the two simulations represent the mode-I fracture characteristics based on TPB test, which show a satisfactory agreement with their experimental counterparts and the simulation result reported in [15] and with the typical three stages as shown in Figure 11. But in Figures 19(b) and 19(c), the curves obtained by the two simulation methods gradually deviate from the curves region obtained by the experiment with the increases of the offset ratio from 0.375 to 0.625.

Through a calibration process aimed to approach the peak load point under the offset ratio $C = 0.5$, two numerical load-displacement curves based on the offset ratios $C = 0.375$ and $C = 0.625$ all show a linear response before reaching the

peak load point, which fail to capture the obvious lower concave stage discussed in Section 3.2. Although the calibrated numerical parameters work well in the scenario of offset ratio $C = 0.5$, the matching characteristic between the experimental and simulation might be failed during other scenarios of offset ratios; this inability is attributed to the softening part of the linear traction-separation law; therefore, the modified traction-separation law needs to be adopted to better describe mixed-mode fracture growth phenomena.

Likewise, as shown in Figures 19(b) and 19(c), the maximum loads simulated by XFEM (see the yellow lines) are larger than the results from the FDEM (see the purple lines), and the values of displacement corresponding to the maximum load point generated from XFEM are smaller than the results from the FDEM. Although there are certain deviations of the load-displacement curves between the simulation and the experiment when the offset ratio is not equal to 0, the trend is consistent. These two simulation methods provide a promising means for the study of the mixed fracture characteristics of compacted soil.

Table 4 summarizes all the maximum loads and corresponding displacements as well as relative errors under $C = 0$, $C = 0.375$, and $C = 0.625$ generated from experimental results and numerical results including XFEM and FDEM. From Table 4, it can be seen that the maximum loads predicted by the FDEM simulation are 31.66 N and 65.15 N under offset ratios $C = 0.375$ and $C = 0.625$, respectively, which are close to the average maximum load of experimental result, i.e., 32.33 N and 63.40 N. However, the maximum loads predicted by the XFEM simulation are 36.86 N and 72.12 N, respectively. The maximum error of load was 14.01% and was predicted by XFEM. The maximum

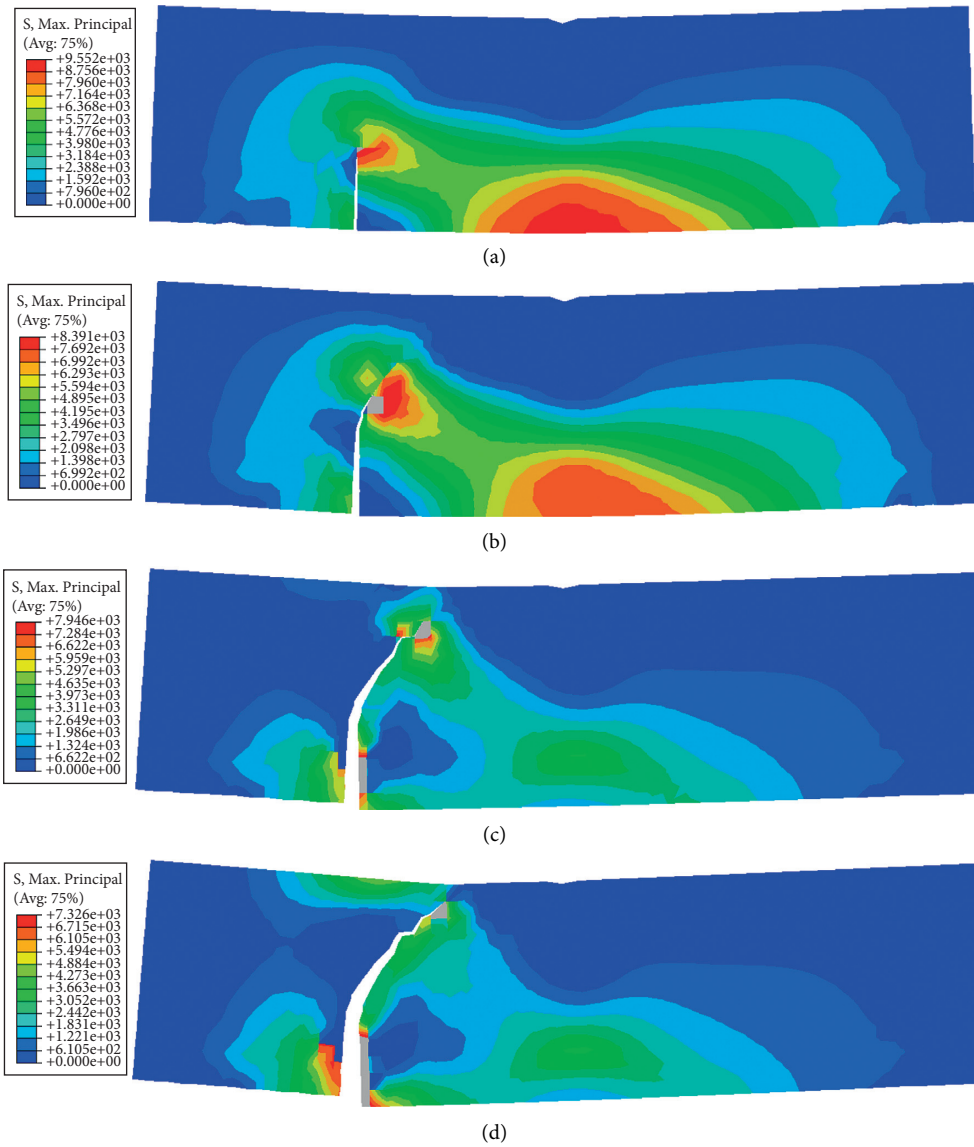


FIGURE 17: The MPSN of the crack propagation process using XFEM. (a) Initial stage; (b) early stage; (c) mid-late stage; and (d) complete crack stage of crack propagation process.

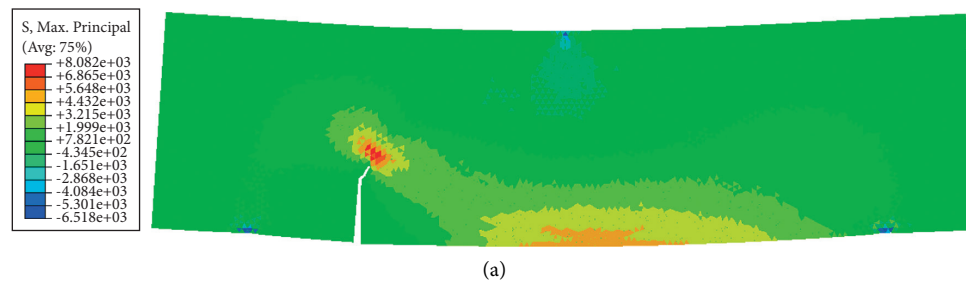


FIGURE 18: Continued.

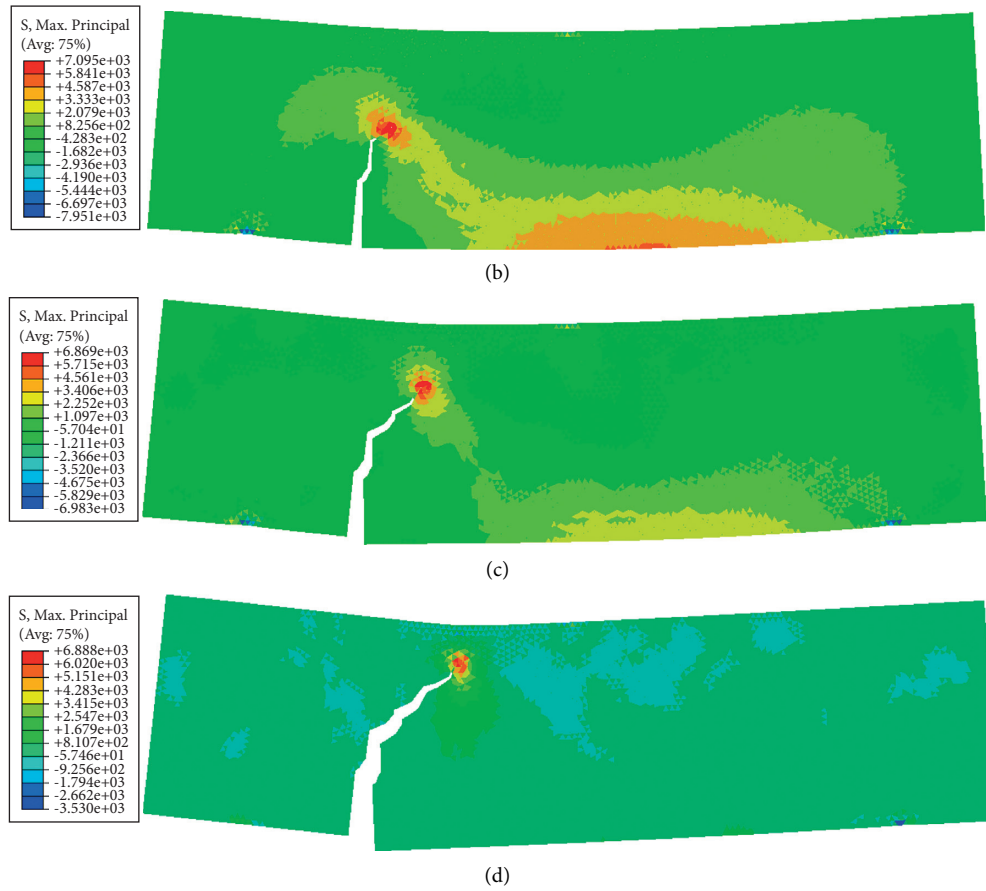


FIGURE 18: The MPSN of the crack propagation process using FDEM. (a) Initial stage; (b) early stage; (c) mid-late stage; and (d) complete crack stage of crack propagation process.

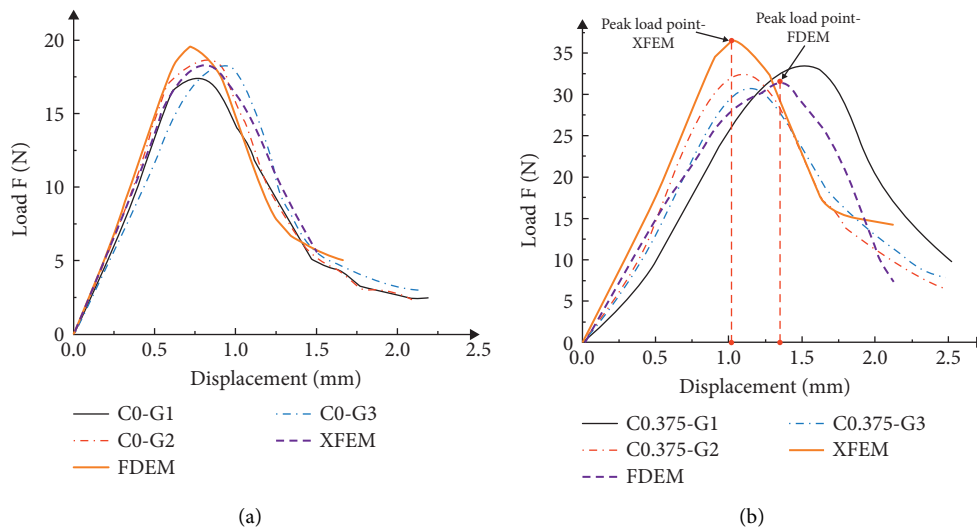


FIGURE 19: Continued.

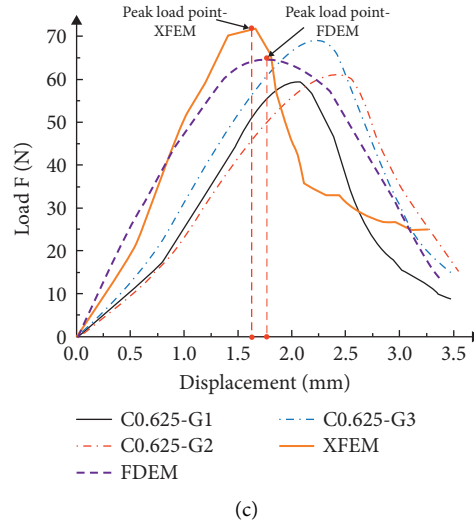


FIGURE 19: Load-displacement curves of simulation and physical test. (a) $C=0$; (b) $C=0.375$; (c) $C=0.625$.

TABLE 4: Comparison of XFEM and FDEM with the experimental test.

| Offset ratio | $C=0$ | | $C=0.375$ | | $C=0.625$ | |
|--------------|--------------------|-------------------|--------------------|-------------------|--------------------|-------------------|
| | Load (N) | Displacement (mm) | Load (N) | Displacement (mm) | Load (N) | Displacement (mm) |
| Experiment | $F_{mave} = 18.15$ | $D_{ave} = 0.85$ | $F_{mave} = 32.33$ | $D_{ave} = 1.24$ | $F_{mave} = 63.40$ | $D_{ave} = 2.18$ |
| XFEM | $F_{max} = 19.26$ | $D = 0.72$ | $F_{max} = 36.86$ | $D = 1.09$ | $F_{max} = 72.12$ | $D = 1.63$ |
| Error-XFEM | 6.12% | 15.29% | 14.01% | 12.10% | 13.75% | 25.23% |
| FDEM | $F_{max} = 18.32$ | $D = 0.83$ | $F_{max} = 31.66$ | $D = 1.35$ | $F_{max} = 65.15$ | $D = 1.76$ |
| Error-FDEM | 0.94% | 2.35% | 2.07% | 8.87% | 2.76% | 19.27% |

error is acceptable. But the minimum error of load was 0.94% and was predicted by FDEM. Therefore, it can be concluded that the peak load value predicted by the FDEM simulation is close to the results generated by physical test. This could be attributed to the fact that the crack-tip singularity and enrichment are not considered and the plasticity of soil is considered elaborately when the CZM in the FDEM is used for simulating the crack initiation and propagation. However, the limitation is that only one kind of soil tightness and moisture content are considered in the simulation.

5. Conclusions

This paper concentrates on the issue of fracture characteristics of clay soil mass, and a TPB test is conducted to investigate the mixed-mode fracture characteristics of the CCB with various offset notches based on experimental and numerical cases; the conclusion of this paper can be summarized with the following points:

- (1) The TPB test of CCB with offset notches indicates that the clay beam specimens will be cracked from the bottom center instead of the preset notch when the offset ratio exceeds 0.717 and the NBHR is 0.33. Therefore, there is an offset ratio threshold

for clay beams with offset notches under a certain NBHR.

- (2) Under a certain NBHR, the peak load and the corresponding displacement of the loading point are increased with the increases of the offset ratio. Offset ratio $C=0.5$ is regarded as a mutation point of the peak load. As the offset ratio increased, the distance between the terminal crack and the centerline increased accordingly, but the initial crack angle of clay beam specimen is decreased.
- (3) The crack propagation morphologies produced from the XFEM and FDEM simulations basically match with the results from the experimental test. The load-displacement curves obtained via FDEM simulations are closer to those from the experimental test with lower error rate of the predicted peak load, that is, 2.07% and 2.76% of offset ratios $C=0.375$ and $C=0.625$, respectively.

In addition, preliminary results of both experimental characterization and numerical simulation have demonstrated that this paper provides a powerful and promising tool for mechanism analysis of the fracture and fragmentation characteristics of soil mass. However, only the NBHR with 0.33 is considered in this work, and the collected data is also limited with small scale view. Consequently, our future

investigations attempt to introduce clay beam specimens with multiple NBHRs and different moisture contents, and large-scale sample and diversity of notch shapes will be considered under various working conditions in practical engineering.

Data Availability

The data that support the findings of this study are included within the article.

Conflicts of Interest

The authors declare that there are no conflicts of interest.

Acknowledgments

This research was funded by the University Science Research Key Project of Anhui Province (Grant no. KJ2019A0172), the State Key Laboratory of Mechanical System and Vibration (Grant no. MSV202015), the National Natural Science Foundation of China (Grant nos. 52005009 and 52105239), and the Key Research and Development Program of Anhui Province (Grant no. 202004e11020003).

References

- [1] A. A. Tagar, C. Ji, Q. Ding, J. Adamowski, F. A. Chandio, and I. A. Mari, "Soil failure patterns and draft as influenced by consistency limits: an evaluation of the remolded soil cutting test," *Soil and Tillage Research*, vol. 137, pp. 58–66, 2014.
- [2] V. Voltr, J. Wollnerová, P. Fuksa, and M. Hruška, "Influence of tillage on the production inputs, outputs, soil compaction and ghg emissions," *Agriculture*, vol. 11, Article ID 11050456, 2021.
- [3] O. B. Aluko, "Finite element aided brittle fracture force estimation during two-dimensional soil cutting," *International Agrophysics*, vol. 22, pp. 5–15, 2008.
- [4] B. Y. Zhang, Q. M. Li, H. N. Yuan, and X. Sun, "Tensile fracture characteristics of compacted soils under uniaxial tension," *Journal of Materials in Civil Engineering*, vol. 27, pp. 1–11, 2014.
- [5] S. Y. Lou, J. He, H. W. Li et al., "Current knowledge and future directions for improving subsoiling quality and reducing energy consumption in conservation fields," *Agriculture*, vol. 11, Article ID 11070575, 2021.
- [6] O. B. Aluko and H. W. Chandler, "A fracture strength parameter for brittle agricultural soils," *Biosystems Engineering*, vol. 93, no. 2, pp. 245–252, 2006.
- [7] J.-J. Wang, J.-G. Zhu, C. F. Chiu, and H. Zhang, "Experimental study on fracture toughness and tensile strength of a clay," *Engineering Geology*, vol. 94, no. 1-2, pp. 65–75, 2007.
- [8] A. L. Amarasiri, S. Costa, and J. K. Kodikara, "Determination of cohesive properties for mode I fracture from compacted clay beams," *Canadian Geotechnical Journal*, vol. 48, no. 8, pp. 1163–1173, 2011.
- [9] J.-J. Wang, S.-Y. Huang, and J.-F. Hu, "Limit of crack depth in KIC testing for a clay," *Engineering Fracture Mechanics*, vol. 164, pp. 19–23, 2016.
- [10] J. Wang, S. Huang, W. Guo, Z. Qiu, and K. Kang, "Experimental study on fracture toughness of a compacted clay using semi-circular bend specimen," *Engineering Fracture Mechanics*, vol. 224, Article ID 106814, 2020.
- [11] C. B. Hu, L. L. Wang, D. S. Cai, W. J. Huang, Z. J. Gong, and L. Shi, "Experimental and numerical investigation on the tensile fracture of compacted clay," *Cmes-Computer Modeling in Engineering and Science*, vol. 123, pp. 283–307, 2020.
- [12] Y. S. Jenq and S. P. Shah, "Mixed-mode fracture of concrete," *International Journal of Fracture*, vol. 38, pp. 123–142, 1988.
- [13] Q. F. Guo, X. H. Wu, M. F. Cai, and S. J. Miao, "Experimental study on the effect of offset notch on fracture properties of rock under three-point bending beam," *Advances in Materials Science and Engineering*, vol. 2020, Article ID 2781928, 7 pages, 2020.
- [14] J. P. Zuo, Y. M. Huang, and L. F. Liu, "Investigation on meso-fracture mechanism of basalt with offset notch based on in-situ three-point bending tests," *Chinese Journal of Rock Mechanics and Engineering*, vol. 32, pp. 740–746, 2013, in Chinese.
- [15] H. T. Tran, Y. N. Wang, G. D. Nguyen, and H. H. Bui, "Modelling 3D desiccation cracking in clayey soils using a size-dependent SPH computational approach," *Computers and Geotechnics*, vol. 116, Article ID 103209, 2019.
- [16] P. F. Liu, "Extended finite element method for strong discontinuity analysis of strain localization of non-associative plasticity materials," *International Journal of Solids and Structures*, vol. 72, pp. 174–189, 2015.
- [17] X. N. Wang, P. Yu, J. L. Yu, and H. Lv, "Simulated crack and slip plane propagation in soil slopes with embedded discontinuities using XFEM," *International Journal of Solids and Structures*, vol. 18, Article ID 0001290, 2018.
- [18] X. Xi, Xu. Wu, QF. Guo, and F. Q. Gong, "Modelling the crack initiation and propagation of notched rock beam under the three-point bending load," *Advances in Civil Engineering*, vol. 2020, Article ID 8810023, 11 pages, 2020.
- [19] W. Zhou, L. W. Tang, X. H. Liu, and M. X. Chen, "Mesoscopic simulation of the dynamic tensile behaviour of concrete based on a rate-dependent cohesive model," *International Journal of Impact Engineering*, vol. 95, pp. 165–175, 2016.
- [20] W. Zhou, W. Yuan, G. Ma, and X. L. Chang, "Combined finite-discrete element method modeling of rockslides," *Engineering Computation*, vol. 33, pp. 1530–1559, 2016.
- [21] G. Ma, Y. Chen, F. H. Yao, and Q. Wang, "Evolution of particle size and shape towards a steady state: insights from FDEM simulations of crushable granular materials," *Computers and Geotechnics*, vol. 112, pp. 147–158, 2019.
- [22] X. D. Chen and H. F. Wang, "Slope failure of noncohesive media modelled with the combined finite-discrete element method," *Appl. Sci-Basel*, vol. 9, p. 579, 2019.
- [23] W. B. Xu, P. W. Cao, and S. K. Cheng, "An experiment on fracture characteristic behaviour of cemented backfill with different offset notch cracks," *Rock and Soil Mechanics*, vol. 39, pp. 1643–1652, 2018, in Chinese.
- [24] Abaqus Analysis User's Manual Version 6.13, *Dassault Systemes Simulia*, Simulia, Providence, Rhode Island, 2013.
- [25] H. Li, J. S. Li, and H. Yuan, "A review of the extended finite element method on macrocrack and microcrack growth simulations," *Theoretical and Applied Fracture Mechanics*, vol. 97, pp. 236–249, 2018.
- [26] A. Munjiza, D. R. J. Owen, and N. Bicanic, "A combined finite-discrete element method in transient dynamics of fracturing solids," *Engineering Computation*, vol. 12, pp. 145–174, 1995.
- [27] A. Abdelaziz, Q. Zhao, and G. Grasselli, "Grain based modelling of rocks using the combined finite-discrete element method," *Computers and Geotechnics*, vol. 103, pp. 73–81, 2018.

- [28] C. B. He, Y. You, D. C. Wang, and J. M. T. Kaji, "The effect of tine geometry during vertical movement on soil penetration resistance using finite element analysis," *Computers and Electronics in Agriculture*, vol. 130, pp. 97–108, 2016.
- [29] M. Li, S. Xu, Y. W. Yang, and J. Tong, "A 3D simulation model of corn stubble cutting using finite element method," *Soil Tillage Research*, vol. 166, pp. 43–51, 2017.
- [30] M. Li, D. H. Chen, S. J. Zhang, and J. Tong, "Biomimetic design of a stubble-cutting disc using finite element analysis," *Journal of Bionic Engineering*, vol. 10, pp. 118–127, 2013.
- [31] Y. S. Wang, X. Z. Hu, L. Liang, and W. C. Zhu, "Determination of tensile strength and fracture toughness of concrete using notched 3-p-b specimens," *Engineering Fracture Mechanics*, vol. 160, pp. 67–77, 2016.